

Multiple Path-Dependent Routes for Phase-Transition Kinetics in Thermoresponsive and Field-Responsive Ultra-soft Colloids

Priti S. Mohanty,^{1,3,*} Payam Bagheri,² Sofi Nöjd,¹ Anand Yethiraj,^{2,†} and Peter Schurtenberger¹

¹*Division of Physical Chemistry, Lund University, SE-221 00 Lund, Sweden*

²*Department of Physics and Physical Oceanography, Memorial University, St. John's, Newfoundland Labrador, Canada, A1B 3X7*

³*School of Applied Sciences, KIIT University, Bhubaneswar 751024, India*

(Received 23 November 2014; published 24 March 2015)

The nature of solid-solid phase transformations has been a long-standing question spanning the fields of metallurgy and condensed-matter physics, with applications from metallic alloys and ceramics to modern shape-memory materials. In spite of the importance of solid-to-solid transformations in many areas of materials science and condensed-matter physics and the numerous experimental and theoretical studies, a deep understanding of the microstructural changes and the underlying kinetic mechanisms is still missing. In this work, we establish a versatile model system composed of micron-scale ionic microgel colloids, where we not only probe the single-particle kinetics in real space and real time but also tune the phase transition in a multiple-parameter space. In the presence of an imposed electric field, a face-centered cubic (FCC) crystal transforms diffusively into a body-centered tetragonal (BCT) crystal via nucleation and growth. In the reverse direction, however, the BCT phase transforms cooperatively into a long-lived metastable body-centered orthorhombic phase, which only relaxes back to the equilibrium FCC when annealed at higher temperatures. The kinetics is thus either diffusive or martensitic depending on the path, and we believe that these two path-dependent transitions provide the first real-space, particle-level insights of diffusive and martensitic transformations, respectively, in a single system.

DOI: [10.1103/PhysRevX.5.011030](https://doi.org/10.1103/PhysRevX.5.011030)

Subject Areas: Materials Science, Soft Matter,
Statistical Physics

I. INTRODUCTION

Understanding phase transformation kinetics in atomic solids is at the basis of numerous technological applications [1,2] in shape-memory materials [3], metals, and alloys [4,5]. Solid-to-solid martensitic transformations are well known in different materials such as steels, shape-memory alloys, and oxide ceramics such as zirconia. Such diffusionless transformations require very little thermal activation energy, and the new crystal structure is obtained by a homogeneous deformation (cooperative motion of all atoms) of the parent structure [4]. In atomic solids, pressure or temperature is used to control the crystal microstructure. For example, fast cooling through the structural transition is used to enhance the strength of steel. The shape-memory effect, where an alloy that is deformed returns to its predeformed state when heated, is used in medical devices.

Viruses also use pressure-induced structural transitions to infect bacteria cells [6]. In contrast to diffusionless martensitic transformations, reconstructive transformations are diffusive; the product crystalline phase is obtained by breaking and rearranging the bonds between atoms, which usually occurs by nucleation and growth [7]. In spite of many studies, both experimental [8–10] and theoretical [6,11], on solid-to-solid transformations, a deep understanding of the microstructural changes and the underlying kinetic mechanisms is still poorly understood, in large part because of the simultaneous challenges of probing atomic time scales and length scales and of controlling the parameters that govern phase transitions.

Colloidal suspensions of spheres interacting via excluded volume plus additional interactions have already provided excellent model systems for different types of phase transitions, including fluid-crystal and gas-liquid phase transitions [12], as well as a range of crystalline phases [13], fluid-fluid cluster phases [14], and glassy states [12,15]. The kinetics of crystal nucleation have been investigated experimentally via scattering [16] and microscopy [17]. Computer simulations have indicated that nucleation kinetics are sensitive to the nature of the interaction potential and the size polydispersity [18,19], and they have demonstrated the importance of thermal fluctuations [20]; quantitative comparisons between experiment and theory are thus challenging.

*Corresponding author.
pritimohanty02@gmail.com

†Corresponding author.
ayethiraj@mun.ca

Published by the American Physical Society under the terms of the Creative Commons Attribution 3.0 License. Further distribution of this work must maintain attribution to the author(s) and the published article's title, journal citation, and DOI.

Studies on solid-to-solid transitions using colloids as a model system have been limited, with studies being carried out in two dimensions [21,22] and in three dimensions [23], but they focused mostly on structural aspects. The ability to induce diffusionless transitions by reversible attractions controlled by DNA handshaking [24] has been reported recently, but a detailed understanding of kinetic mechanisms and when and why metastable intermediates occur in three-dimensional solid-solid transitions remains elusive to experiment. Finally, a two-step nucleation pathway was recently identified in a quasi-two-dimensional solid-solid transition [25]; it is exceedingly important to examine whether the observed two-step pathway is indeed generic in three dimensions.

Ionic microgel colloidal particles [26,27] can easily deform and/or overlap, and the interparticle spacing a_s can be smaller than the particle diameter σ , such that realistic particle-number densities n can result in very large “effective” packing fractions ($\phi_{\text{eff}} = \pi\sigma^3 n/6$). They are thus an interesting alternative to the previously studied hard-sphere-like and charged colloidal systems. Their loosely cross-linked swollen structure results in an “ultrasoft” interaction potential that allows extensive particle overlap and results in a very rich phase diagram with complex crystalline structures [26]. At zero field, the effective interaction potential between ionic microgels varies from long-range screened Coulomb (Yukawa-like) at low densities (where the average interparticle distance $a_s > \sigma$, the diameter of the particle) to short-range soft repulsive at extremely high packing fractions (where particles start overlapping, i.e., where $a_s < \sigma$). This interaction potential has been experimentally verified recently [28].

In addition, these ionic microgels contain a large amount of confined counterions and correspondingly exhibit a large frequency-dependent electric polarizability, the details of which are currently being investigated via impedance spectroscopy. They are thus exceptionally responsive to an external electric field and exhibit various field-induced transitions such as fluid-to-string and crystal-to-crystal transitions at low effective volume fractions $\phi_{\text{eff}} < \phi_{cp}$, and crystal-to-glass and glass-to-arrested phase-separated states at $\phi_{\text{eff}} > \phi_{cp}$, where ϕ_{cp} refers to (hard-sphere) close packing [29,30]. This is in contrast to typical hard-sphere colloids, which respond to a high-frequency ac external electric field as dielectric spheres in a dielectric medium. The effect of this field on the colloids can be modelled by the point-dipolar approximation [31] and is described in Ref. [32].

With increasing temperature, the size of the microgel particles decreases. At the same time, we expect that the effective soft repulsive interaction potential at distances smaller than the particle diameter gets stiffer with increasing temperature. This has already been reported for neutral microgels [33]. Although this behavior will be similar for all types of microgels, the temperature dependence of the particle size and stiffness of the potential will vary depending on the cross-linking density, charge density, etc.

In the current study, we probe the kinetics of a field-induced colloidal phase transition from a face-centered cubic (FCC) to a body-centered tetragonal (BCT) crystal, in three dimensions, and both in the forward and reverse directions by increasing and decreasing the electric field strength, respectively.

II. RESULTS AND DISCUSSION

Our colloidal system consists of monodisperse fluorescently labeled ultrasoft poly(*N*-isopropylacrylamide) (PNIPAM)-based ionic microgel particles in aqueous suspension. Most experiments were carried out at constant number density and at 20 °C, corresponding to an effective volume fraction $\phi_{\text{eff}} = 1.36$; see Methods for details of sample conditions.

First, we investigate the kinetics of the field-induced FCC-to-BCT transition in the presence of an ac electric field of amplitude $E = 0.105 \text{ V}/\mu\text{m}$ in a bulk suspension. Although our system is three dimensional, the time series are limited to two (X and Y) dimensions in order to access faster dynamics. Most of our experiments are carried out at a distance of 10 particle diameters from the substrate. Experiments were also performed at a much greater distance from the substrate (up to 30 particle diameters), and no systematic difference was observed in the phase-transformation phenomena in this range. However, we have refrained from showing images at larger depths due to the fact that the image quality was noticeably worse at the high particle concentration used in the experiments. This is due to a small difference in refractive index between the PNIPAM particles and the water, which results in significant transmission losses for the fluorescence intensity from the particles at large depths caused by scattering. It should also be noted that microscopy experiments are intrinsically limited (because of the working distance of the high-resolution objectives, 100x) to distances less than 100 microns.

Figure 1(a) shows two-dimensional (2D) confocal laser scanning micrographs at six different times (from a few seconds to several minutes); the complete dynamics may be observed in a time-series movie (see Supplemental Material 35). The structural transformation is quantified via the local 6-fold and 4-fold bond-order parameters ψ_6 and ψ_4 (see Methods section for details). Regions of high ψ_6 and ψ_4 are colored red and blue, respectively, in the Voronoi color map [Fig. 1(b)], while disordered (defect-rich) regions with both low ψ_6 and ψ_4 are colored white. Further, the population fractions (f_6 , f_4 , and f_{dis}) for high- ψ_6 , high- ψ_4 , and disordered regions may be obtained as a function of time after the electric-field quench [Fig. 1(c)].

The initial, zero-field parent phase (FCC) consists of approximately 95% of the particles exhibiting strong 6-fold symmetry coexisting with 5% of defect-rich regions (marked by white dashed lines). Melting begins in the defect-rich regions, which get wider with time with the emergence of local disordered regions consisting of

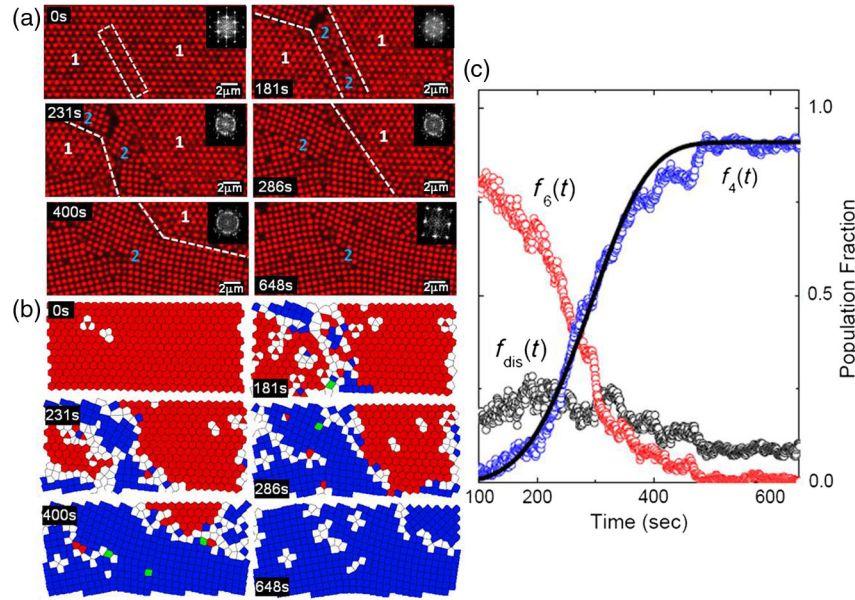


FIG. 1. Overview of the kinetics of the field-induced FCC to BCT transition for $E = 0.105 \text{ V}/\mu\text{m}$, $\phi_{\text{eff}} = 1.36$ and $T = 20^\circ\text{C}$. (a) Time-dependent 2D confocal images taken in the bulk at distances of 10 particle diameters from the substrate. The field direction is perpendicular to the XY image plane. The numbers 1 and 2 correspond to regions of 6-fold and 4-fold symmetry, respectively, and the white dashed lines are drawn to highlight regions with defects. The inset figures, obtained via a 2D Fourier transform of the images, show predominantly 6-fold symmetry for the first 3 minutes and predominantly 4-fold symmetry after about 7 minutes. (b) Voronoi map color coded with bond-order parameters for the images shown in (a). Red: $\psi_6 > 0.7$; blue: $\psi_4 > 0.55$; white: $\psi_6 < 0.7$ and $\psi_4 < 0.7$; green: $\psi_6 > 0.7$ and $\psi_4 > 0.7$. The latter rarely or never occurs. (c) Population fractions of 6-fold [$f_6(t)$], 4-fold [$f_4(t)$], and disordered [$f_{\text{dis}}(t)$] regions as a function of time (t). Notably, $f_4(t)$ shows a sharp increase near $t = 200 \text{ s}$ and a plateau after about 600 s. The population fraction of the product phase [$f_4(t)$] is fitted to the Avrami equation for nucleation and growth, with exponent $\alpha = 4.0$.

particles in a disordered fluid state and in strings along the Z direction. The regime with “fluid + strings” is short: By $t = 181 \text{ s}$, squares with 4-fold symmetry have nucleated from the disordered region and coexist with 65% of the 6-fold symmetry regions; correspondingly, the population fraction (f_{dis}) has a maximum here [Fig. 1(c)].

At this time, there is a sharp increase in f_4 (with a discontinuous change in slope), attributable to nucleation of the product phase, which is followed by a more gradual increase over the time scale of minutes which can be attributed to growth and coarsening of the BCT phase, with most of the regions having 4-fold symmetry at $t = 400 \text{ s}$ and a near complete transformation by $t = 648 \text{ s}$.

The population fraction at very short times ($t = 0\text{--}100 \text{ s}$) could not be calculated because of a tiny drift of the microscope stage resulting in two planes being simultaneously visible, as can be observed by inspection of the original movie (Supplemental Material 35).

The growth curve of the product phase is found to be in remarkable agreement with the Avrami equation [solid line in Fig. 1(c)] for nucleation and growth, $f_4 \sim [1 - \exp(-Kt^\alpha)]$, where the power-law exponent $\alpha \sim 4.0$. The Avrami exponent $\alpha = 4$ is consistent with polyhedral grain growth in three dimensions. The physical significance is that at early stages of phase transformation, the total crystal volume V is the product of the number of growth

nuclei N_g and their volume V_g : N_g is proportional to t , while the grain volume V_g is proportional to t^3 [34].

Second, we study the phase transition kinetics after switching off the electric field (Fig. 2). Here, the dynamics is completely different, as demonstrated by images at different times [Fig. 2(a)] and through a time-series movie (see Supplemental Material 35). Particles move cooperatively relative to their neighbors and transform from 4-fold to 6-fold symmetry within a very short time as compared to the case of the FCC-to-BCT transition (seconds as opposed to minutes). This is seen particularly clearly in the Voronoi color maps, as well as in the bond-order plots, Fig. 2 [(b) and (c), respectively]. The transition from 4-fold to 6-fold in-plane symmetry is very clear, and it appears not to be initiated at defects or grain boundaries. Instead, at $t = 40 \text{ s}$, the nucleated 6-fold symmetry regions are homogeneously distributed all over the parent phase [see the Voronoi map at $t = 40 \text{ s}$ in Fig. 2(b)]. These regions grow very fast: At $t = 70 \text{ s}$, we already see a steady state, with 75% of the regions having 6-fold symmetry. The growth of 6-fold in-plane symmetry is once again tested against the Avrami form [solid line in Fig. 2(c)]. Here, the power-law exponent $\alpha \sim 8.5$ ($\alpha \gg 4$), which suggests that the classical nucleation and growth mechanism is not relevant here. At longer times ($t = 90 \text{ s}$, 100 s and 115 s), there is no change: f_6 and f_4 show a sharp

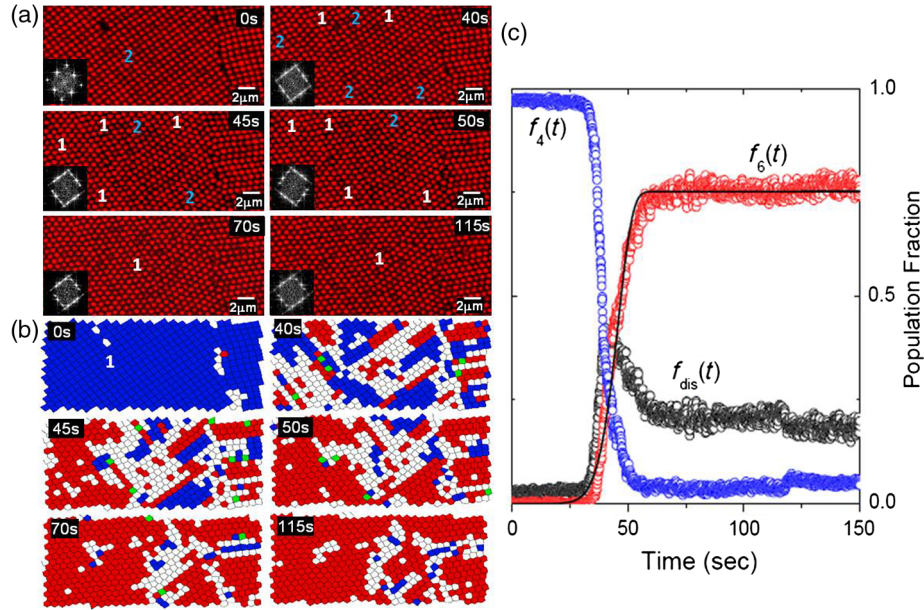


FIG. 2. Phase-transition kinetics in the reverse direction after the field is switched off. $\phi_{\text{eff}} = 1.36$, $T = 20^\circ\text{C}$. (a) Time-dependent 2D confocal images taken in the bulk at distances of 10 particle diameters from the substrate. The numbers 1 and 2 again highlight regions of 6-fold and 4-fold symmetry, respectively. The inset image Fourier transforms only show strong 4-fold symmetry for the first 30 s. (b) Voronoi color map for the images shown in (a). Red: $\psi_6 > 0.7$; blue: $\psi_4 > 0.55$; white: $\psi_6 < 0.7$ and $\psi_4 < 0.7$; green: $\psi_6 > 0.7$ and $\psi_4 > 0.7$. It is clear that the disappearance of 4-fold symmetry in the reverse direction is much more rapid than the structural change in the forward direction. (c) Population fractions of 6-fold [$f_6(t)$], 4-fold [$f_4(t)$], and disordered [$f_{\text{dis}}(t)$] regions as a function of time (t) show a sharp decrease in f_4 , coupled with a sharp increase in f_6 ; f_{dis} exhibits a maximum near 40 s. The evolution of 6-fold symmetry after the field is turned off is fitted with the Avrami equation yielding $\alpha = 8.5$ and is thus inconsistent with a simple nucleation and growth model.

decrease and increase with a narrow range of coexistence. Above $t = 50$ s, f_6 and f_4 attain a plateau, while f_{dis} initially increases from a very low value, then reaches a maximum, followed by a decrease to a constant nonzero value at long times.

We examined the 6-fold symmetric structure observed after 70 s in Figs. 2(a) and 2(b) carefully in three dimensions (3D). Figures 3(a)–3(c) show two-dimensional (2D) images of the initial zero-field FCC structure, the field-induced BCT structure, and the new field-off structure (top row). The bottom row of Figs. 3(a)–3(c) shows three-layer projections, where three consecutive layers in the Z stack are assigned as red, green, and blue pseudocolors. The initial parent structure has 6-fold symmetry in 2D [Fig. 3(a), top] and ABC stacking [Fig. 3(a), bottom]. For the FCC structure at $\phi_{\text{eff}} = 1.36$, the lattice spacing $a = a_s \sqrt{2} \sim 1.21 \mu\text{m}$, where a_s is the average interparticle distance estimated from the first peak position of the pair-correlation function $g(r)$. The BCT crystal can be constructed by placing strings of particles into two interpenetrating square lattices ($a = b$), where the particles in the strings are displaced by $c/2$ along the Z direction. Figure 3(b) (top panel) shows 4-fold symmetry, and each single particle in the 2D image is a projection of a string. This is why the three-layer projection (bottom) is identical to the 2D image. From the 2D and 3D $g(r)$, the lattice

spacing in the X - Y plane ($a = b$) and along the Z direction (c) are calculated to be $a = b \sim 1.05 \mu\text{m}$ and $c \sim 0.82 \mu\text{m}$, respectively. In Fig. 3(c), the 2D image again coincides with the three-layer projection demonstrating that the crystal is composed of strings that have not melted after the field is switched off. We thus find that, surprisingly, this zero-field crystal is clearly not FCC. By explicit measurement in 3D, this structure is identified to be a body-centered orthorhombic (BCO) crystal with lattice spacings $a = 0.92 \mu\text{m}$, $b = 1.2 \mu\text{m}$ in the X - Y plane and $c = 0.86 \mu\text{m}$ along the Z direction.

The metastable BCO structure is long-lived: It did not melt 8 hours after the field was switched off (see Fig. 1 in Ref. [35]). The reason for this kinetic arrest is likely the ultrasoft nature of the potential, allowing for significantly more particle overlap along the field direction: In the BCT phase, along the field direction, the average interparticle separation ($c \sim 0.82 \mu\text{m}$) is much smaller than the hydrodynamic diameter ($\sigma = 1.06 \mu\text{m}$) of the particle in the swollen state. It is remarkable that this anisotropy persists after the field is turned off, leading to a large separation of time scales for in-plane kinetics (seconds) and out-of-plane kinetics (hours).

To speed up the kinetics, we “annealed” the BCO state at 31.5°C . We then observe (Fig. 4) that the BCO state transforms into a FCC phase that persists upon cooling

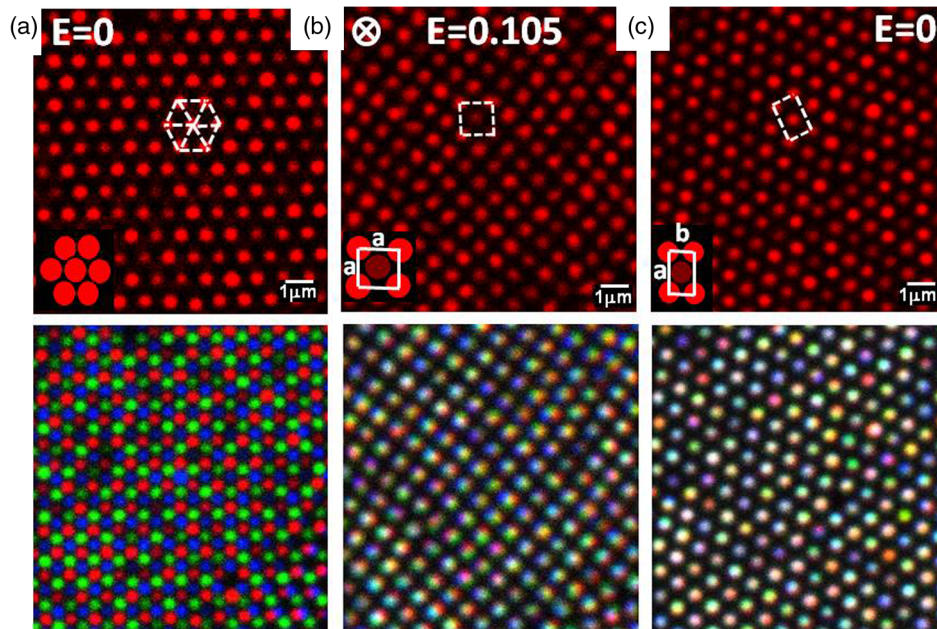


FIG. 3. Two-dimensional image and three-layer projections (top and bottom, respectively) of (a) the initial zero-field FCC, (b) the field-induced BCT, and (c) the field-off structure. The three-layer projections are constructed by merging three consecutive layers in the stack after assigning them as pseudocolors RGB.

back to 20 °C. Annealing in this system is complicated. The temperature change, in terms of an increase in $k_B T$, is modest, so thermal annealing is not likely to be predominant. The temperature change also simultaneously changes particle diameter (and thus changes ϕ_{eff}) and makes the inter-particle interaction stiffer. We believe that the last factor is likely to be the most important for the reasons outlined next.

We also carried out field experiments in the forward and reverse directions and at the same temperature ($T = 20^\circ\text{C}$) but at lower packings, $\phi_{\text{eff}} = 0.6$. At this low ϕ_{eff} , the zero-field structure is a coexistence of FCC with disordered fluid, and with an increasing field in the forward direction, a low-density BCT phase is seen, similar to our previous results [30]. However, when we switch off the electric field, we observe a BCO phase that coexists

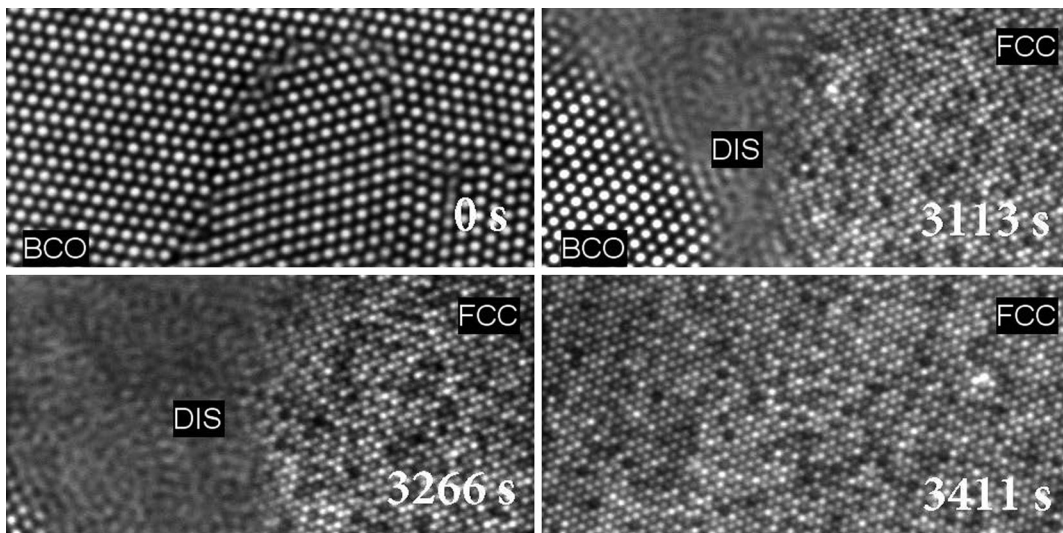


FIG. 4. Annealing of the arrested BCO phase at 31.5 °C for approximately 1 hour returns it to FCC. Images from left to right are Z-projected images (averaged over several frames) obtained from 3D Z stacks at times $t = 0, 3113 \text{ s}, 3266 \text{ s},$ and 3411 s . At intermediate times, the BCO state transits through a coexistence regime, BCO + Fluid (DIS) + FCC. In the projected image, the region where the particles are diffusive and in the fluid phase appears blurred.

with the disordered fluid phase (see Supplemental Material 35). The Supplemental Material 35 shows the kinetics for the same experiment in the forward direction (fluid-crystal coexistence to BCT). This demonstrates, convincingly, that it is the intrachain particle overlap (rather than the overall packing) that stabilizes the arrest of the BCO state even at low ϕ_{eff} .

However, there exists a threshold ($\phi_{\text{eff}} = 0.43$) below which no long-lived BCO metastable states were seen. Here, the equilibrium high-field BCT structure completely melts back to the fluid state via string aggregates at intermediate $E = 0.047 \text{ V}/\mu\text{m}$ and string + fluid at $E = 0.034 \text{ V}/\mu\text{m}$ (see Supplemental Material [35]).

Finally, we discuss the nature of the phase-transition kinetics in the forward (field-induced) and reverse (field-off) directions. This field-induced FCC-to-BCT transition is not martensitic. Colloidal analogues of martensitic transitions have been found in different systems [21–24]. The FCC-to-BCT transition resembles polymorphic (diffusive or re-constructive) transformations in metals and ceramic materials, which occur by heterogeneous nucleation and thermally activated growth. Defects or grain boundaries act as heterogeneous nucleation sites for the product phase. The FCC-to-BCT transformation may provide the first direct real-space evidence of a diffusive transformation in three dimensions.

In the reverse direction, the BCT-to-BCO-to-FCC structural sequence exhibits three interesting phenomena. The BCT-to-BCO transition is diffusionless: It is a colloidal analogue of well-known martensitic transformation, which occurs as expected [1,3] through a cooperative movement of all particles. Second, this transition results in a long-lived metastable state. This martensitic BCT-BCO transition is reversible, in spite of the fact that the forward transition is not. The unexpected reverse transition scenario indicates that crystal-to-crystal transformations in three dimensions exhibit richer phenomena than in quasi-two-dimensional systems [25], arising from the possibility for different time scales along different crystal directions in anisotropic materials. Control over temperature and number density allows a detailed study of this metastability. The nature of solid-solid phase transformations has been a long-standing question, spanning the fields of metallurgy and condensed-matter physics, and we believe that the current system of ionic microgels can serve as an ideal model system to gain further insight.

III. METHODS

A. Colloids

We use monodisperse, fluorescently labeled, PNIPAM-based ionic microgels as a model system for our current study. Details of synthesis are described elsewhere [30]. The samples were fully deionized using an ion-exchange resin prior to experiments. The ultrasoft particles have a

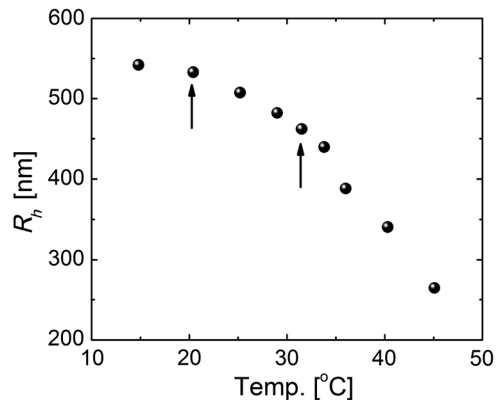


FIG. 5. Average hydrodynamic radius R_h measured by dynamic light scattering as a function of temperature for a highly diluted microgel suspension. The confocal microscopy studies were carried out at 20 °C and 31.5 °C, indicated by the arrows.

dense core and a fuzzy shell: The core radius (from static light scattering) $R_{\text{SLS}} = 357 \text{ nm}$, while the hydrodynamic radius (from dynamic light scattering) $R_{\text{DLS}} = 530 \text{ nm}$ at $T = 20 \text{ °C}$. The swelling behavior was studied by means of dynamic light scattering. The hydrodynamic radius R_h was measured (Fig. 5) as a function of temperature using a modulated 3D cross-correlation instrument (LS instruments, Switzerland) at a wavelength of 632 nm and with noninteracting highly dilute suspensions. The data were analyzed using a first-order cumulant analysis to obtain the translational diffusion coefficient D_0 , and the hydrodynamic radius was then calculated using the Stokes-Einstein equation, $D_0 = k_B T / (6\pi\eta R_h)$, where k_B is the Boltzmann constant, T is the absolute temperature, and η is the solvent viscosity. Measurements were done in an angular range $30^\circ \leq \theta \leq 50^\circ$, where θ is the scattering angle, and averaged over three different angles after having verified that the decay rate exhibits a Q^2 dependence indicating purely diffusive motions. With increasing temperature, the radius decreases, reflecting the typical thermoresponsive nature of PNIPAM-based microgels. For neutral PNIPAM microgel, the volume phase transition (VPT) occurs around 33 °C. However, in our case, the VPT is shifted to higher temperatures. This shift is due to the fact that the swelling of ionic microgels is strongly influenced by the combined effects of two contributions, a strong Coulomb repulsion between neighboring ionic groups within the microgel and the osmotic pressure of the counterions.

B. Sample conditions

Confocal laser-scanning-microscopy experiments were carried out at 20 °C and at constant number density (which corresponds to an effective volume fraction, $\phi_{\text{eff}} = 1.36$). Some experiments under different conditions were also carried out: at lower number densities ($\phi_{\text{eff}} = 0.43$ and 0.53 at 20 °C) and at higher temperature ($\phi_{\text{eff}} = 0.9$ at 31.5 °C).

The electric field, at a constant frequency of 100 kHz (high enough to safely avoid electrohydrodynamic flow), was applied along the Z direction perpendicular to the image plane, and all the observations were made in the XY -image plane.

C. Bond-order parameters

In order to quantify structure, a Voronoi tessellation of the time-series images is first constructed, and a 2D local bond-order parameter is defined as

$$\Psi_s = \left| \frac{1}{N} \sum_{j=1}^N e^{si\theta_j} \right|, \quad (1)$$

where N is the number of the nearest neighbors of a lattice point; s can be either 4 or 6; and θ_j is the angle between the line connecting a nearest neighbor to the lattice point, and a reference axis. The color maps in Fig. 1(b) denote regions with high 6-fold symmetry ($\psi_6 > 0.7$, red), high 4-fold symmetry ($\psi_4 > 0.55$, blue), and disordered regions (with both $\psi_6 < 0.7$ and $\psi_4 < 0.55$, white). Using these thresholds, population fractions f_6 , f_4 , and f_{dis} are then defined.

ACKNOWLEDGMENTS

P. S. acknowledges financial support from the science faculty of Lund University and the Swedish Research Council (Project No. 621-2011-4338). This work was supported in part by the Natural Sciences and Engineering Research Council of Canada (NSERC).

P. M., A. Y., and P. S. designed the study; P. M. and S. N. synthesized the particles and performed the experimental research; P. M. and P. B. analyzed the data; and P. M., A. Y., and P. S. jointly discussed and wrote the paper.

-
- [1] E. Salje, *Phase Transitions in Ferroelastic and Co-elastic Crystals*, 3rd ed. (Cambridge University Press, Cambridge, England, 1993).
 - [2] G. Olson and W. Owen, *Martensite*, 3rd ed. (ASM International, Materials Park, OH, 1992).
 - [3] K. Otsuka and C. Wayman, *Shape Memory Materials*, 3rd ed. (Cambridge University Press, Cambridge, England, 1998).
 - [4] D. Porter, K. E. Easterling, and M. Sherif, *Phase Transformations in Metals and Alloys*, 3rd ed. (CRC Press, Boca Raton, FL, 2009).
 - [5] H. Bhadeshia and R. Honeycombe, *Steels: Microstructure and Properties: Microstructure and Properties*, 3rd ed. (Butterworth-Heinemann, UK, 2011).
 - [6] K. Bhattacharya, S. Conti, G. Zanzotto, and J. Zimmer, *Crystal Symmetry and the Reversibility of Martensitic Transformations*, *Nature (London)* **428**, 55 (2004).
 - [7] M. Barsoum, *Fundamentals of Ceramics*, 3rd ed. (CRC Press, Boca Raton, FL, 2003).

- [8] K. Jacobs, D. Zaziski, E. C. Scher, A. B. L. Herhold, and A. P. Alivisatos, *Activation Volumes for Solid-Solid Transformations in Nanocrystals*, *Science* **293**, 1803 (2001).
- [9] Y. Song, X. Chen, V. Dabade, T. W. Shield, and R. D. James, *Enhanced Reversibility and Unusual Microstructure of a Phase-Transforming Material*, *Nature (London)* **502**, 85 (2013).
- [10] M. Bocanegra-Bernal, S. D. D. la Torre, E. C. Scher, A. B. L. Herhold, and A. P. Alivisatos, *Phase Transitions in Zirconium Dioxide and Related Materials for High Performance Engineering Ceramics*, *J. Mater. Sci.* **37**, 4947 (2002).
- [11] M. Rao and S. Sengupta, *Nucleation of Solids in Solids: Ferrites and Martensites*, *Phys. Rev. Lett.* **91**, 045502 (2003).
- [12] P. N. Pusey and W. van Meegen, *Phase Behavior of Concentrated Suspensions of Nearly Hard Colloidal Spheres*, *Nature (London)* **320**, 340 (1986).
- [13] A. Yethiraj and A. van Blaaderen, *A Colloidal Model System with an Interaction Tunable from Hard Sphere to Soft and Dipolar*, *Nature (London)* **421**, 513 (2003).
- [14] A. Stradner, H. Sedgwick, F. Cardinaux, W. C. K. Poon, S. U. Egelhaaf, and P. Schurtenberger, *Equilibrium Cluster Formation in Concentrated Protein Solutions and Colloids*, *Nature (London)* **432**, 492 (2004).
- [15] E. R. Weeks, J. C. Crocker, A. C. Levitt, A. B. Schofield, and D. A. Weitz, *Three-Dimensional Direct Imaging of Structural Relaxation Near the Colloidal Glass Transition*, *Science* **287**, 627 (2000).
- [16] T. Palberg, *Colloidal Crystallization Dynamics*, *Current Opinion Colloid Interface Sci.* **2**, 607 (1997).
- [17] U. Gasser, E. R. Weeks, A. Schofield, P. N. Pusey, and D. A. Weitz, *Real-Space Imaging of Nucleation and Growth in Colloidal Crystallization*, *Science* **292**, 258 (2001).
- [18] S. Auer and D. Frenkel, *Quantitative Prediction of Crystal-Nucleation Rates for Spherical Colloids: A Computational Approach*, *Annu. Rev. Phys. Chem.* **55**, 333 (2004).
- [19] L. Fillion, R. Ni, D. Frenkel, and M. Dijkstra, *Simulation of Nucleation in Almost Hard-Sphere Colloids: The Discrepancy between Experiment and Simulation Persists*, *J. Chem. Phys.* **134**, 134901 (2011).
- [20] J. Russo and H. Tanaka, *The Microscopic Pathway to Crystallization in Supercooled Liquids*, *Sci. Rep.* **2**, 1 (2012).
- [21] J. A. Weiss, D. W. Oxtoby, D. G. Grier, and C. A. Murray, *Martensitic Transition in a Confined Colloidal Suspension*, *J. Chem. Phys.* **103**, 1180 (1995).
- [22] K. Zhao, R. Bruinsma, and T. G. Mason, *Entropic Crystal-Crystal Transitions of Brownian Squares*, *Proceedings of the Indian National Science Academy Part B, Biological sciences* **108**, 2684 (2011).
- [23] A. Yethiraj, A. Wouterse, B. Groh, and A. van Blaaderen, *Nature of an Electric-Field-Induced Colloidal Martensitic Transition*, *Phys. Rev. Lett.* **92**, 058301 (2004).
- [24] M. T. Casey, R. T. Scarlett, W. B. Rogers, I. Jenkins, T. Sinno, and J. C. Crocker, *Driving Diffusionless Transformations in Colloidal Crystals Using DNA Handshaking*, *Nature Commun.* **3**, 1209 (2012).

- [25] Y. Peng, F. Wang, Z. Wang, A. M. Alsayed, Z. Zhang, A. G. Yodh, and Y. Han, *Two-Step Nucleation Mechanism in Solid-Solid Phase Transitions*, *Nat. Mater.* **14** 101 (2015).
- [26] D. Gottwald, C. Likos, G. Kahl, and H. Löwen, *Phase Behavior of Ionic Microgels*, *Phys. Rev. Lett.* **92**, 068301 (2004).
- [27] D. M. Heyes and A. C. Branka, *Interactions between Microgel Particles*, *Soft Matter* **5**, 2681 (2009).
- [28] J. Riest, P. S. Mohanty, P. Schurtenberger, and C. N. Likos, *Coarse-Graining of Ionic Microgels: Theory and Experiment*, *Z. Phys. Chem.* **226**, 711 (2012).
- [29] P. S. Mohanty, A. Yethiraj, and P. Schurtenberger, *Deformable Particles with Anisotropic Interactions: Unusual Field-Induced Structural Transitions in Ultrasoft Ionic Microgel Colloids*, *Soft Matter* **8**, 10819 (2012).
- [30] S. Nöjd, P. S. Mohanty, P. Bagheri, A. Yethiraj, and P. Schurtenberger, *Electric Field Driven Self-Assembly of Ionic Microgels*, *Soft Matter* **9**, 9199 (2013).
- [31] M. Parthasarathy and D. Klingenberg, *Electrorheology: Mechanisms and Models*, *Mater. Sci. Eng.* **R17**, 57 (1996).
- [32] A. Yethiraj, *Tunable Colloids: Control of Colloidal Phase Transitions with Tunable Interactions*, *Soft Matter* **3**, 1099 (2007).
- [33] Y. Han, N. Y. Ha, A. M. Alsayed, and A. G. Yodh, *Melting of Two-Dimensional Tunable-Diameter Colloidal Crystals*, *Phys. Rev. E* **77**, 041406 (2008).
- [34] M. Avrami, *Kinetics of Phase Change. II. Transformation-Time Relations for Random Distribution of Nuclei*, *J. Chem. Phys.* **8**, 212 (1940).
- [35] See the Supplemental Material at <http://link.aps.org/supplemental/10.1103/PhysRevX.5.011030> for details about I) Synthesis and characterization of microgel particles. II) Time dependent studies of the arrested BCO phase at 20 °C. III) Melting of the BCT phase at low density by decreasing the field strength E at 20 °C and information about the Supplementary Movie.